PNAS Nexus, 2024, 3, pgae446
https://doi.org/10.1093/pnasnexus/pgae446
Advance access publication 4 October 2024
Research Report

Mapping uterine calcium dynamics during the ovulatory cycle in live mice

David J. Combs [a,b], Eric M. Moult[b], Sarah K. England[c] and Adam E. Cohen [b,d,*]

[a]Department of Anesthesiology, Perioperative and Pain Medicine, Brigham and Women's Hospital, Harvard Medical School, Boston, MA 02115, USA
[b]Department of Chemistry and Chemical Biology, Harvard University, Cambridge, MA 02138, USA
[c]Department of Obstetrics and Gynecology, Center for Reproductive Health Sciences, Washington University School of Medicine, St. Louis, MO 63110, USA
[d]Department of Physics, Harvard University, Cambridge, MA 02138, USA
*To whom correspondence should be addressed: Email: cohen@chemistry.harvard.edu
Edited By Myles Alderman III

Abstract

Uterine contraction patterns vary during the ovulatory cycle and throughout pregnancy, but prior measurements have produced limited and conflicting information on these patterns. We combined a virally delivered genetically encoded calcium reporter (GCaMP8m) and ultra-widefield imaging in live nonpregnant mice to characterize uterine calcium dynamics at organ scale throughout the estrous cycle. Prior to ovulation (proestrus and estrus), uterine excitations primarily initiated in a region near the oviduct, but after ovulation (metestrus and diestrus), excitations initiated at loci homogeneously distributed throughout the organ. The frequency of excitation events was lowest in proestrus and estrus, higher in metestrus, and highest in diestrus. These results establish a platform for mapping uterine activity and demonstrate that an anatomically localized trigger for uterine excitations depends on the estrous cycle phase.

Significance Statement

Uterine contractions are essential for mammalian reproduction. Elevation in cytoplasmic calcium concentration triggers uterine muscle contractions, but the organ-level patterns of calcium dynamics and the mechanisms driving these patterns are unknown. We imaged calcium dynamics of the uterus in live nonpregnant mice and found a rich repertoire of excitation modes, including estrous cycle-dependent shifts in the distribution of initiation sites and activity patterns. A technique to map uterine calcium in vivo opens the door to studying regulation of uterine contractions in models of health and disease.

Introduction

Uterine contractions support important biological functions. In pregnancy, they are central to labor and delivery, as well as postpartum hemostasis (1). Outside of pregnancy, uterine contractions assist in fertilization, implantation, and the clearance of menstrual debris, as reviewed by Aguilar and Mitchell (2). Aberrant uterine contractility is implicated in preterm birth, dystocia, postpartum hemorrhage, infertility, dysmenorrhea, and endometriosis, all common conditions, many of which carry significant morbidity or mortality.

Cellular and molecular studies have identified many of the ion channels and other proteins central to uterine myocyte electrophysiology (for a review, see (3)). However, it is not clear how these components produce tissue-scale activity, and how that activity is coordinated and controlled during ovulation and pregnancy. As contractions in pregnancy are quasi-periodic (4) and nonpregnancy contractions vary in frequency and origin throughout the ovulatory cycle (5–11), prior work sought evidence for uterine pacemakers (12). However, without high-quality organ-scale maps of uterine activity patterns, the search for a putative uterine pacemaker is difficult. Prior studies have investigated pacing by interstitial cells and by specialized muscle cells (13, 14), but it is not clear whether uterine contractions are triggered by specific cell types or if they emerge from the collective activity of the muscle as a whole; and to what extent the initiation sites are anatomically localized vs broadly distributed (15). High-resolution activity maps in live animals could pinpoint the loci driving organ-wide activity and could inform on the molecular mechanisms underlying the cycle-dependent changes in activity patterns.

Measurement of calcium dynamics with genetically encoded calcium indicators presents a promising approach to this challenge. These tools are readily deployed at organ scale in living animals and have been used in brain (16), mammary ducts (17), skeletal muscle (18), and heart (19, 20). In combination with cell type-specific drivers, these indicators report the activity of cellular subpopulations within a complex tissue.

Competing Interest: The authors declare no competing interests.
Received: September 3, 2024. **Accepted:** September 16, 2024

Here, we use the genetically encoded calcium indicator jGCaMP8m to map myometrial calcium dynamics across an entire uterine horn in live mice at different stages of the estrous cycle. These measurements showed cycle-dependent changes in propagation velocity, locus of initiation, and event rate. During ovulation (proestrus and estrus), activity was aperiodic and primarily originated from the ovarian end of the uterine horn. After ovulation (metestrus and diestrus), activity originated throughout the uterine horn. Establishment of a mouse model for uterine calcium imaging in vivo holds promise for future studies of the molecular and cellular factors governing these dynamics.

Methods

For a more detailed description of all procedures, see Supplemental Methods.

Mouse strains and maintenance

All animal procedures adhered to the NIH Guide for the care and use of laboratory animals and were approved by the Harvard University Institutional Animal Care and Use Committee. Progesterone receptor (PR)-Cre$^{+/-}$ mice (JAX 017915) were generously provided by the strain's creator, Nirao Shah at Stanford University (21). Anti-Müllerian hormone receptor 2 (AMHR2)-Cre$^{+/-}$ mice (22) were generously provided by the laboratory of Kara McKinley at Harvard University. Ai148 mice (JAX 030328), for cre-dependent GCaMP6f expression, were obtained from the Jackson Laboratory. All mice were housed in standard conditions (reverse 12-h light/dark cycles, with water and food ad libitum). For all experiments involving injection of viruses carrying *cre*-dependent payloads, genotyped female heterozygotes were generated from crosses with wild-type C57BL/6 mice obtained from Charles River Laboratories. Genotyped PR-Cre$^{+/-}$; Ai148D$^{+/-}$ or AMHR2-Cre$^{+/-}$; Ai148D$^{+/-}$ double heterozygotes were created by the crossing of respective parental strains. All genotyping was performed by Transnetyx.

Vaginal cytology and estrous cycle staging

Vaginal cytology and estrous staging were performed by vaginal lavage with 50–100 μL of phosphate-buffered saline (PBS) using a micropipette tip and suction bulb followed by crystal violet staining of freshly dried cytology preparations, as previously described (23). All cytology specimens were collected ∼1 h before lights off. For virus-injected female mice, first cytology specimens were not obtained until at least 21 days postoperatively to allow for surgical recovery and restoration of uninterrupted light–dark cycling. Estrous staging was determined by daily vaginal cytology over at least 5 days prior to measurement. Calcium imaging of each estrous stage was only performed when the day-of-measurement cytology matched the cytology expected based on the prior days' specimens.

Virus injection surgery

AAV9 virus expressing jGCaMP8m under a CAG promoter was obtained from Addgene (162381-AAV9). This gene delivery method was selected for its low immunogenicity (24). For injections, prealiquoted frozen virus was thawed and diluted to 5×10^{12} genome copies/mL in a total volume of 10 μL, containing 10% (v/v) of trypan blue dye to visualize spread of the injectate and to guide adjustments to the injection location(s).

For the virus injection procedure (see also Supplemental Methods), 8–12-week-old heterozygous PR-Cre$^{+/-}$ female mice were anesthetized, a vertical incision was made left paramedian to the midline to access the peritoneal cavity, and the left uterine horn was identified. Injections were made using home-fabricated micropipettes (Sutter P1000) with beveled tips created with a home-built micropipette polisher. Micropipettes were mounted in a microinjection pump (WPI Nanoliter 2010), positioned with a micromanipulator (WPI, MP-285), and injection volumes controlled with a microsyringe pump controller (WPI, Micro4). After loading of viral injectate and positioning of the micropipette near the uterine horn, injections were performed by gentle grasping of the mesometrium with microforceps and simultaneous advancement of the micropipette into the uterine horn. Virus was injected in two 300 nL volumes at 50 nL/s at each injection site with 5–10 s of postinjection time before pipette removal to assess injectate spread and prevent leakage. Injection sites consisted of 12–16 evenly spaced locations along the anterior face of the organ longitudinal axis from the left half of the uterine body (junction of the two uterine horns) to the horn end adjacent to the oviduct. Following injections, the fascial layer was closed with interrupted 5–0 monocryl sutures and the skin closed with wound clips.

Animal preparation for live-animal imaging

We allowed a minimum of 3 weeks between virus injection and imaging. Animals were anesthetized at 3% isoflurane and then maintained at 1% isoflurane, a concentration shown not to impair uterine contractions (25). A midline abdominal incision was made to expose the peritoneal cavity and the bladder drained transmurally. A pair of custom 3D-printed (Anycubic Photon Mono) semicircular (16 mm diameter and 8 mm height) abdominal retractors were positioned at the inferior and superior borders of the abdominal incision, with extension of the incision to accommodate retractor insertion (∼3.5 cm). Soaked gauze strips were adjusted to sit between the retractor and the abdominal wall to protect the wall surface from drying or damage from the retractors (Fig. S3A). Care was taken to avoid stretching or applying instruments to the uterus to avoid mechanical stimuli. The time from induction of anesthesia to collection of the last image < 90 min and operative time was < 60 min (40 min from start of recording last image), to ensure that the preparation remained stable during measurement. It was not feasible to image the entirety of both uterine horns simultaneously, so for animals where both the injected horn and the contralateral horn were imaged, gauze and retractors were adjusted to optimize the view of the imaged horn. After each animal imaging session, the animal was euthanized.

Calcium imaging

The stage for in vivo imaging was positioned below the objective of a custom optical setup for widefield imaging previously described (26, 27). For recordings of jGCaMP8m dynamics, widefield illumination was supplied (0.1–0.2 mW mm^{-2}) with a 470-nm light emitting diode. Excitation light was reflected off a large (65 × 80 × 3 mm) dual band (509–540 and 614–700 nm, Alluxa) dichroic mirror. Fluorescence was separated from back-scattered excitation by a 65-mm-diameter 520/35-nm band-pass emission filter. Imaging was done via a 1× objective lens, numerical aperture 0.25 (Olympus MVPLAPO 1X). Data were captured on a Kinetix sCMOS Camera (Teledyne Photometrics) at 5 Hz framerate through a camera lens repurposed as a tube lens (VS Technology Co, VS-50085/M42). The iris was set to achieve the focal depth needed to image the convex organ surface and to accommodate any anteroposterior displacement along the organ longitudinal axis. The adjoining oviduct, junction of the two

uterine horns and (often 1–2 mm) of the contralateral horn could also be imaged simultaneously. Illumination and acquisition timing was controlled using custom MATLAB software (https://www.luminosmicroscopy.com) via a National Instruments DAQ interface. For details on image processing, see Supplemental Methods.

Immunostaining and confocal microscopy

For immunostaining of uterine rings (see Supplemental Methods), rings were permeabilized (0.1% Triton X-100 in PBS), blocked (1% bovine serum albumin in PBS with 0.1% Tween 20), and then incubated with the primary antibody in fresh blocking solution for 1 h at room temperature. After secondary antibody incubation (1 h, room temperature), rings were incubated for 5 min with 300 nM DAPI, washed, and mounted on glass slides. Primary antibodies were: chicken anti-green fluorescent protein (Abcam, ab13970, 1:500) and rabbit anti-alpha smooth muscle actin (Abcam, ab124964, 1:500). Secondary antibodies were donkey antichicken Alexa Fluor 488 (Jackson Immunology 703-545-155, 1:1,000) and antirabbit Alexa Fluor 647 (Abcam, ab150075, 1:1,000).

Imaging of fixed immunostained uterine rings was performed on an LSM 700 Confocal Microscope and Zen v3.2 software (Zeiss). Image stacks were converted to maximal intensity projection images in ImageJ.

Statistics

Plots were created in MATLAB. All boxplots show median and inter-quartile range (IQR) with whiskers indicating 1.5 × IQR. The numbers of independent repeat experiments performed in different animals are displayed as n values. For statistical comparisons of features between estrous stages that proved significantly different ($P < 0.05$) by one-way ANOVA, Tukey's test was used with a multiple-comparison procedure. For paired comparison of the injected and contralateral horn, two-tailed paired t test was performed. Sample size was determined by the practical limitations of the experiments.

Results

Adeno-associated virus injection enables in vivo myometrial transgene expression

To map uterine calcium dynamics, we developed methods for in vivo transgene delivery and calcium imaging. Adeno-associated virus (AAV)-mediated transgene expression has not been reported in uterine smooth muscle. Plasmid-based uterine muscle-specific promoters have not been described, and no transgenic mice have been created that express site-specific recombinases exclusively in uterine smooth muscle. We therefore chose a commercially available AAV with payload comprising the universal CAG promoter and Cre-dependent expression of the calcium indicator jGCaMP8m (28). We chose the AAV9 capsid serotype, which has been successfully used for in vivo transgene expression in skeletal and cardiac muscle (29). We used PR-Cre mice to target expression to myometrium (21). Virus was injected into the anterior face of the uterine horn along its longitudinal axis via an open abdominal surgery (Fig. 1; Methods). In virus-injected animals, estrous staging was determined by vaginal cytology (Figs. 1 and S1; Methods).

Virus injection led to expression of jGCaMP8m in the injected, but not the contralateral, uterine horn (Fig. S2). Despite injections only in the anterior face of the uterine horn, jGCaMP8m expression spread around the circumference of the organ. jGCaMP8m expressed in both circular and longitudinal muscle layers (Fig. S2). Consistent with the known tissue-specific expression pattern of Cre in PR-Cre mice (30), jGCaMP8m also expressed in the endometrium. Expression lasted for at least 12 weeks after injection. Some virus-injected mice ($n = 9$) were set aside to test for fertility instead of being used for in vivo imaging. These mice all achieved pregnancy within 3 months, the same timeframe used for in vivo imaging in other mice, confirming that the virus injection and jGCaMP8m expression did not impair fertility.

Attempts at crossing two Cre driver lines (PR-Cre and AMHR2-Cre) with a Cre-dependent GCaMP6s reporter mouse line to drive whole-uterus reporter expression produced female offspring expressing calcium indicator throughout their uteri, but these animals had atrophic uteri and were infertile, so this strategy was not pursued further (Fig. S4, Supplemental Methods, Supplemental Discussion). To delay transgenic expression of GCaMP6s until maturity, we tried to use a doxycycline-dependent transgenic reporter mouse (Supplemental Methods). Pups fed doxycycline chow to suppress reporter expression experienced high (~50%) mortality. Though adults had normal-looking uteri, they were infertile. Attempts to deliver transgenes by direct electroporation into wild-type uteruses were also not successful. Efforts to load calcium-sensitive dyes directly into the uterus in vivo did not produce sufficient dye loading to resolve calcium signals.

In addition to live-animal imaging (see below), we tried to image whole-uterus explants. Despite an extensive search of conditions (Supplemental Methods), explanted uteri, although alive, showed markedly less spontaneous activity than in vivo, consistent with prior reports (31) (Fig. S5).

Wide-area live-animal calcium imaging reveals estrous-related changes in calcium dynamics

We imaged uterine calcium dynamics in vivo in mice expressing virally delivered jGCaMP8m (Fig. 1B–E and Movies S1–S4). We performed several control experiments to validate the in vivo preparation. Uterine horns expressing jGCaMP8m appeared anatomically normal compared with noninjected controls within the same animal (Fig. S3B and C). The spontaneous event rate did not change between the beginning and end of the recording sessions, confirming the stability of the preparation (Fig. S3D). The spontaneous event rate (as detected via tissue motion) was not significantly different between the injected and noninjected horns within the same animal, confirming that viral expression of jGCaMP8m did not perturb the endogenous dynamics (Fig. S3E). Fluorescence dynamics in the injected horn were significantly larger in magnitude than in the contralateral horn, confirming that the fluorescence signals came from jGCaMP8m (Fig. S3F and G).

We observed different kinds of calcium excitation events. Some excitations comprised circumferential rings of elevated calcium, coupled with a local reduction in organ diameter (Fig. 1B and E). These propagated slowly along the uterine axis. Other excitations increased calcium in axially elongated strips, coupled with long-axis shortening (Fig. 1C and D). These propagated quickly along the uterine axis. We provisionally associate these events to independent activation of the circular and longitudinal muscle layers, respectively. However, many events did not show clear axial or circular morphology and instead appeared to have mixed excitation of both muscle layers (Fig. S6). We therefore did not attempt to classify events by muscle layer.

Recordings of calcium dynamics were taken from mice in all four estrous stages ($n = 5$ mice per stage). Qualitatively, videos from proestrus and estrus mice had markedly less activity than those from metestrus and diestrus mice (Movies S1–S4). To

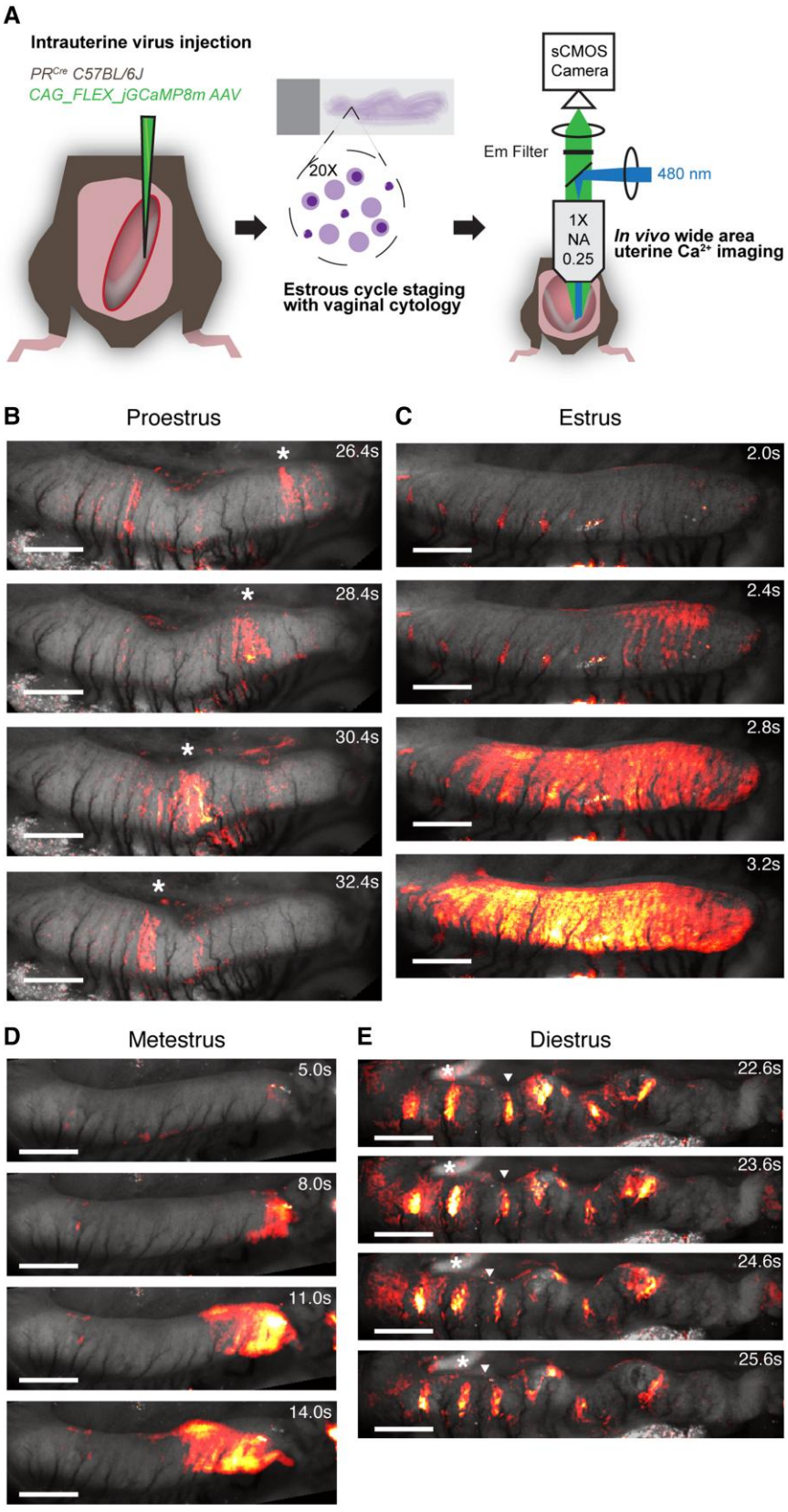

Fig. 1. Live-animal wide-area uterine calcium imaging during estrous cycle. A) Experimental scheme. Left panel: The uterus was injected with AAV virus encoding GCaMP8m. Middle: Estrous stage was determined with vaginal cytology. Right: Uterine calcium dynamics were imaged on an ultra-widefield microscope. Images from movies of calcium dynamics with the change in fluorescence in color overlaid on a grayscale image of the basal fluorescence for B) proestrus, C) estrus, D) metestrus, and E) diestrus. Asterisks (B) and arrowheads (E) mark propagating bands of activity in successive images. Scale bars 1 mm in all images.

analyze differences in activity among the four estrous stages, we developed an image processing pipeline to extract and quantify uterine excitation events (Fig. S7 and Supplemental Methods). In brief, we used motion-tracking and nonrigid deformation algorithms to undo the effects of tissue motion. We then defined a piecewise linear contour along the axis of the expressing uterine horn, and projected the fluorescence dynamics onto this axis, leading to fluorescence kymographs comprising one time dimension and one spatial dimension along the uterine axis (Fig. 2A). This procedure discarded information about circumferential calcium dynamics, but visual inspection of the movies showed that most of the propagation was axial. We then used a combination of machine learning-based (32) and feature-based algorithms to identify calcium events and to quantify their locus of initiation, propagation speed, propagation duration, and full width at half maximum (Figs. 2 and 3, Methods).

We compared the properties of calcium events across estrous stages. Propagation velocities in proestrus (2.3 ± 1.1 mm/s, median $\pm$ SD) and estrus (1.2 ± 0.9 mm/s) were faster than in metestrus (0.13 ± 0.01 mm/s) and diestrus (0.12 ± 0.02 mm/s; $P < 0.01$, one-way ANOVA, Fig. 2C). Median event propagation distances (as magnitudes) in proestrus and estrus appeared slightly higher than in metestrus and diestrus, but this did not achieve statistical significance (Fig. 2D). To look at the duration of events at a given location (i.e. at a particular kymograph spatial coordinate), event-triggered averages were generated from their leading half maxima. FWHM, a measure of the duration of calcium elevation at a given location, of these mean event traces did not differ by estrous stage (Fig. 2E). Event rates (number of events/total recording time, Fig. 3A) were much lower for proestrus (0.01 ± 0.004 Hz) and estrus (0.009 ± 0.01 Hz) than for metestrus (0.09 ± 0.02 Hz) and diestrus (0.17 ± 0.05 Hz; $P < 1 \times 10^{-6}$). Table 1 summarizes these observations.

A region with pacer-like features exists in proestrus and estrus, but not metestrus and diestrus

In the heart, an anatomically and molecularly distinct pacemaker region coordinates the beating of the whole organ. Whether an analogous structure exists in the uterus has been controversial (4, 12). We searched for pacemaker-like dynamics in the uterine Ca^{2+} signal. Two key elements of a pacing system are localization and periodicity. That is, events may originate from a single locus or from multiple loci and may occur periodically or at irregular intervals.

To examine where events initiated, we mapped our data onto a normalized uterine horn longitudinal axis, and then sorted event loci of initiation (LOIs) into deciles along this axis. During estrus and proestrus, activity primarily initiated from regions near the oviduct, with 82 and 74% of events, respectively, emerging from two deciles closest to the oviduct (Fig. 3B). In contrast, events in metestrus and diestrus showed an even distribution of LOIs across the uterine horn (Fig. 3B). The spatially distributed LOIs in diestrus and metestrus appeared equally likely to propagate toward the oviduct or toward the cervix, whereas those in proestrus and estrus showed a strong directional bias to propagate in the cervical direction (Fig. 3C).

Although portions of some kymographs showed periodic activity emanating from a particular locus, this periodicity did not appear stable. The inter-event intervals were widely distributed for all estrous stages (Fig. 3D). To examine the temporal structure of events in more detail, we generated power spectra from kymographs of recordings at each estrous stage (Fig. 4A–C). The power spectra of dynamics in the uterine horn did not have any peaks, indicating absence of periodicity in each estrous stage. To confirm that we could detect a periodic signal, we examined the oviduct, which, in a subset of samples, exhibited jGCaMP8m signal, likely acquired from viral injections into the oviductal end of the uterine horn. Consistent with previous reports of myosalpinx contractions in the oviduct paced by interstitial cells of Cajal (33), the oviductal calcium signal was highly periodic with a typical frequency of 0.15 Hz (Fig. 4). However, synchrony of oviductal and uterine activity was not maintained in any estrous stage (Fig. 4C).

Discussion

We developed a protocol to express transgenes in the mouse uterine myometrium and for live-animal imaging of calcium dynamics across the organ. Uterine calcium activity changed throughout the estrous cycle. Proestrus and estrus stages featured rare, fast-propagating, and short-lived activity which started near the oviduct. In contrast, metestrus and diestrus exhibited more frequent, slower-moving, and longer-lasting Ca^{2+} excitations which initiated throughout the organ and which propagated with equal probabilities toward the cervix and the ovaries.

Patterns of uterine activity are sensitive to the tissue preparation. A key feature of our preparation is that it measures in vivo dynamics under close-to-physiological conditions. Prior measurements of live rodent uterine activity (7, 34, 35) imposed substantial uterine stretch, possibly altering endogenous dynamics (36). In our measurements, computational correction for tissue motion relieved the requirement to physically immobilize the tissue. Whole-uterus explants also did not reproduce in vivo activity patterns, possibly due to the absence of circulating factors or paracrine or neural stimuli. Prior experiments with dissected preparations cut across uterine muscle fibers (8–11), creating damage that likely disrupted endogenous patterns of electrical activity.

The physiological basis of the shift toward ovarian-end initiation during proestrus and estrus is not known. One plausible explanation could be a spatially dependent shift in the intrinsic properties of the myocytes throughout the estrous cycle. Our results suggest that future work should compare the electrophysiological and transcriptomic properties of the ovarian vs cervical ends of the uterus throughout the estrous cycle. Single-cell transcriptomic analysis identified four myocyte subtypes in the uterus (37), but the spatial patterns of gene expression have not yet been mapped throughout the estrus cycle.

The high propagation velocities and low event rates we observed in proestrus and estrus are consistent with previously reported increases in gap junction expression in those phases (38). Increases in gap junction conductance are expected to speed electrical conduction, but also to increase electrotonic loading of nascent initiation sites and thereby to decrease the event rate (39).

Prior studies reported seemingly inconsistent patterns of estrous cycle-dependent uterine dynamics in rodents. Early electromyogram (EMG) studies in live rodents showed drops in activity from estrus to diestrus (5, 6). Dodds et al. (10) used tension and motion measurements on uterine explants from mice and also reported diestrus as the most quiescent phase. In contrast, Wray and Noble (9) studied tension and calcium in rodent myometrial strips and found diestrus to be the most active stage, consistent with our results. A recent study of organ motion in uterine

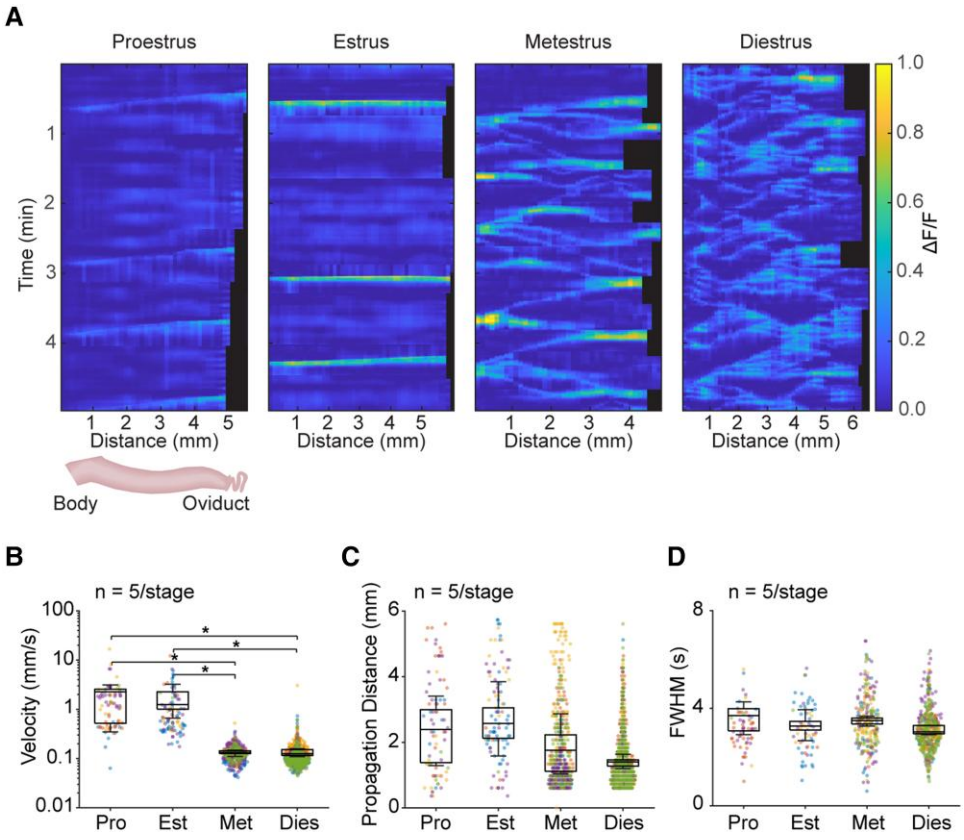

Fig. 2. Uterine calcium dynamics vary by estrous stage. A) Representative kymographs of fold-change in fluorescence for each estrous stage. B) Kymograph segments showing fast (arrowhead) and slow (asterisk) conduction modes in same specimen. For each panel in (A), the right-most spatial coordinate is closest to the oviduct. Black regions indicate organ length contractions, leading to no data from the ovarian end. Event-wise distributions of B) propagation velocity, C) distance, and D) full width at half maximum (FWHM). Box plots represent IQR (25th, 50th, and 75th percentile) with whiskers representing 1.5× IQR. Swarm plot points represent values from individual calcium events. Colors identify events occurring in the same animal. Proestrus (Pro), estrus (Est), metestrus (Met), and diestrus (Dies) stages had $n = 5$ animals per stage. For statistics (B), $P < 0.01$ (one-way ANOVA), with multiple-comparison testing by Tukey's test where $^*P < 0.05$.

explants also identified diestrus as the most active stage (40). These differences may be due to the use of different measurement modalities. Tissue motion, intrauterine pressure, electrical recordings, and calcium imaging all probe different aspects of myometrial activity and may have different sensitivities to different modes of excitation. For example, simultaneous EMG and intrauterine pressure measurements showed that not all electrical activity produced pressure changes (6). Microelectrode arrays provided in-layer spatial resolution and showed that estrus explants had more synchronous activity than diestrus explants (11), and the degree of synchrony among the muscle fibers may influence the extent of mechanical contraction.

We hypothesize that the highly localized circular-layer calcium events we observed primarily during diestrus and metestrus produced only small global changes in tension, pressure, and organ profile. Indeed, in our diestrus videos, slowly propagating circular-layer events only decreased uterus diameter by 0.1 mm ± 0.06 mm (median ± SD; $n = 10$ events, 5 animals), whereas circular-layer events in proestrus or estrus decreased organ diameter by 0.4 mm ± 0.15 mm ($n = 10$ events, 6 animals).

The biological significance of the distinct modes of uterine excitation we observed is not clear. While mice, like most mammals, do not menstruate, proliferating endometrial tissues degenerate and are ultimately resorbed in diestrus (41). We speculate that bidirectionally propagating activity in metestrus and diestrus may assist endometrial breakdown. Nonmechanical effects of calcium excitation events are also possible, e.g. via calcium-mediated changes in gene expression (42).

Despite the novel *in vivo* imaging methodology we introduced, there remain some limitations. Widefield imaging did not provide depth-resolved information, preventing clear assignment of activity to muscle layers. Two-photon (43) or structured illumination (44) microscopies could provide depth-dependent information, though data analysis in the presence of 3D tissue deformations will be a challenge. Another limitation is that calcium imaging is downstream of membrane electrical excitation, and voltage measurements could provide more detailed information about the mechanisms of bioelectrical excitation. Recent progress in applying voltage imaging and optogenetics in cardiac muscle (20) suggests that similar tools may be applicable in the uterus.

Another potential limitation is that the degree of anatomical and functional homology between rodent and human uterine activity is controversial (1, 45). Unlike mice, women have a single fused uterine cavity with an innermost muscle layer abutting the endometrium (*stratum subvasculare*) with largely circular fibers and the remaining myometrium largely disordered (2, 46). As with the rodent estrous cycle, human myometrial activity varies over the menstrual cycle, with the strongest activity occurring at menstruation (47). The best-characterized activity patterns in human nonpregnant myometrium are those of uterine peristalsis in the *stratum subvasculare*, primarily studied with cine ultrasound (48–50). We did not observe similar-looking patterns in mice, though

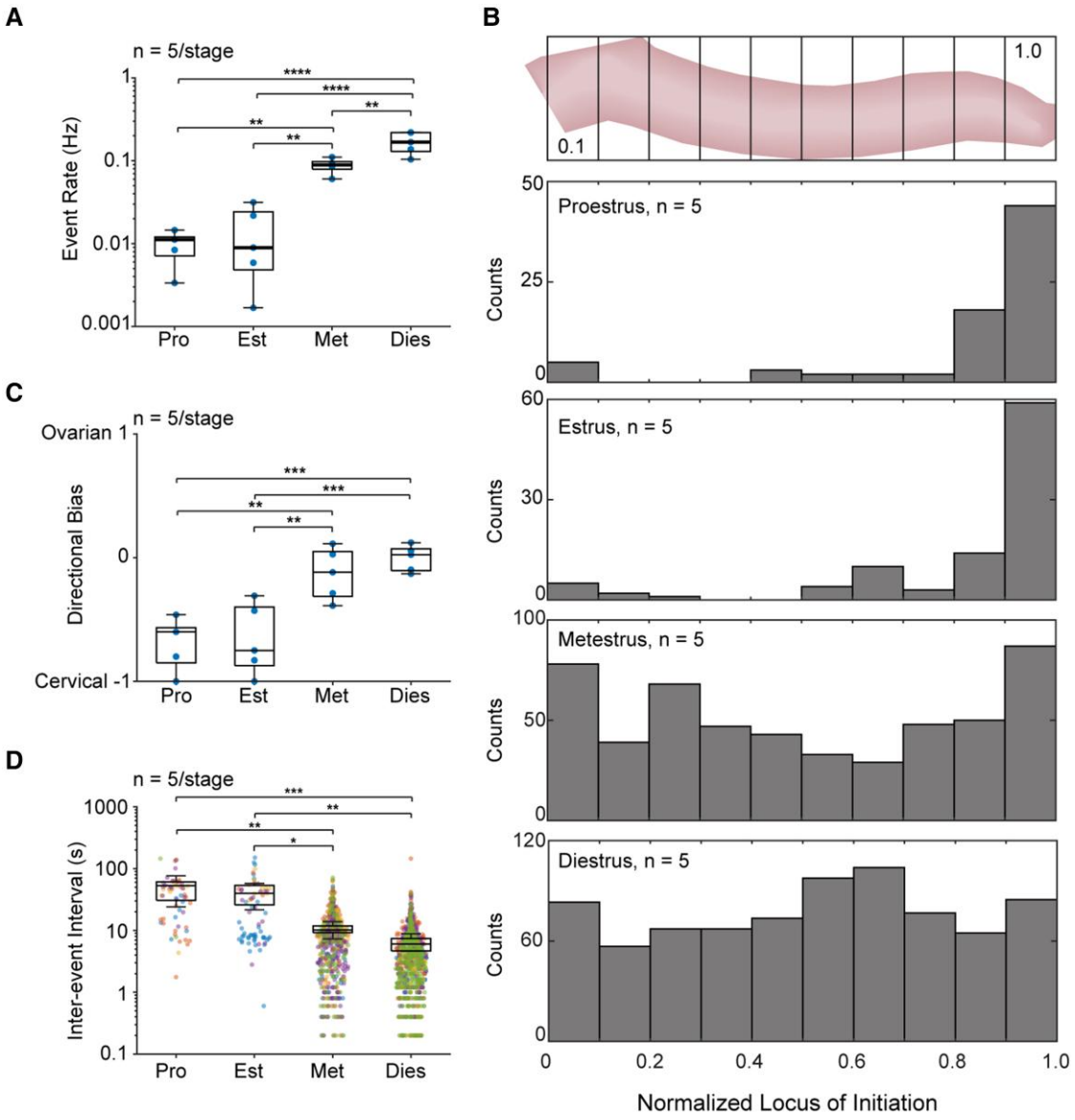

Fig. 3. Frequency, direction, and loci of initiation of uterine calcium events vary by estrous stage. Distributions of A) event rate and B) loci of initiation. Counts represent all events across five animals per stage. C) Propagation directional bias. D) Inter-event interval. In (A) and (C), data points represent individual animals; in (D), data points represent pairs of successive calcium events. Like-colored points in (D) identify events occurring in the same animal. Box plots represent IQR (25th, 50th, and 75th percentile) with whiskers representing 1.5 × IQR. Proestrus (Pro), estrus (Est), metestrus (Met), and diestrus (Dies) stages had $n = 5$ animals per stage. For statistics, A) $P < 1 \times 10^{-6}$, C) $P < 1 \times 10^{-4}$, and D) $P < 0.002$ by one-way ANOVA; multiple-comparison testing by Tukey's test where $^{*}P < 0.05$, $^{**}P < 0.01$, $^{***}P < 0.001$, and $^{****}P < 1 \times 10^{-4}$.

Table 1. Velocities and event rates of calcium events.

Cycle stage	Velocity (mm/s)	Event rate (Hz)	Origin
Proestrus	2.3 ± 1.1[a]	0.01 ± 0.004	Near oviduct
Estrus	1.2 ± 0.9	0.01 ± 0.01	Near oviduct
Metestrus	0.13 ± 0.01	0.09 ± 0.02	Distributed
Diestrus	0.12 ± 0.02	0.17 ± 0.05	Distributed

[a]Median and SDS.

the use of different measurement modalities makes precise comparison difficult.

Despite the difference in anatomy, humans and rodents share many regulatory and molecular elements of uterine biology (1, 45), making rodents a useful model for studying molecular and cellular mechanisms of uterine activity. Rodent models of obstetric and gynecologic conditions enable experiments that are not possible in humans (51–58). Our study emphasizes the importance of using in vivo preparations to faithfully characterize spontaneous activity patterns. Our preparation opens a path to studying uterine physiology, pathophysiology, and pharmacology in vivo. In future studies, we plan to investigate the mechanisms that underlie estrous-related changes and to adapt our approaches to study the myometrium throughout pregnancy and in models of disease.

Acknowledgments

The authors thank Shahinoor Begum and Andrew Preecha for technical assistance and mouse husbandry, Kara McKinley and Nirao Shah for generously providing transgenic animals, Ronald

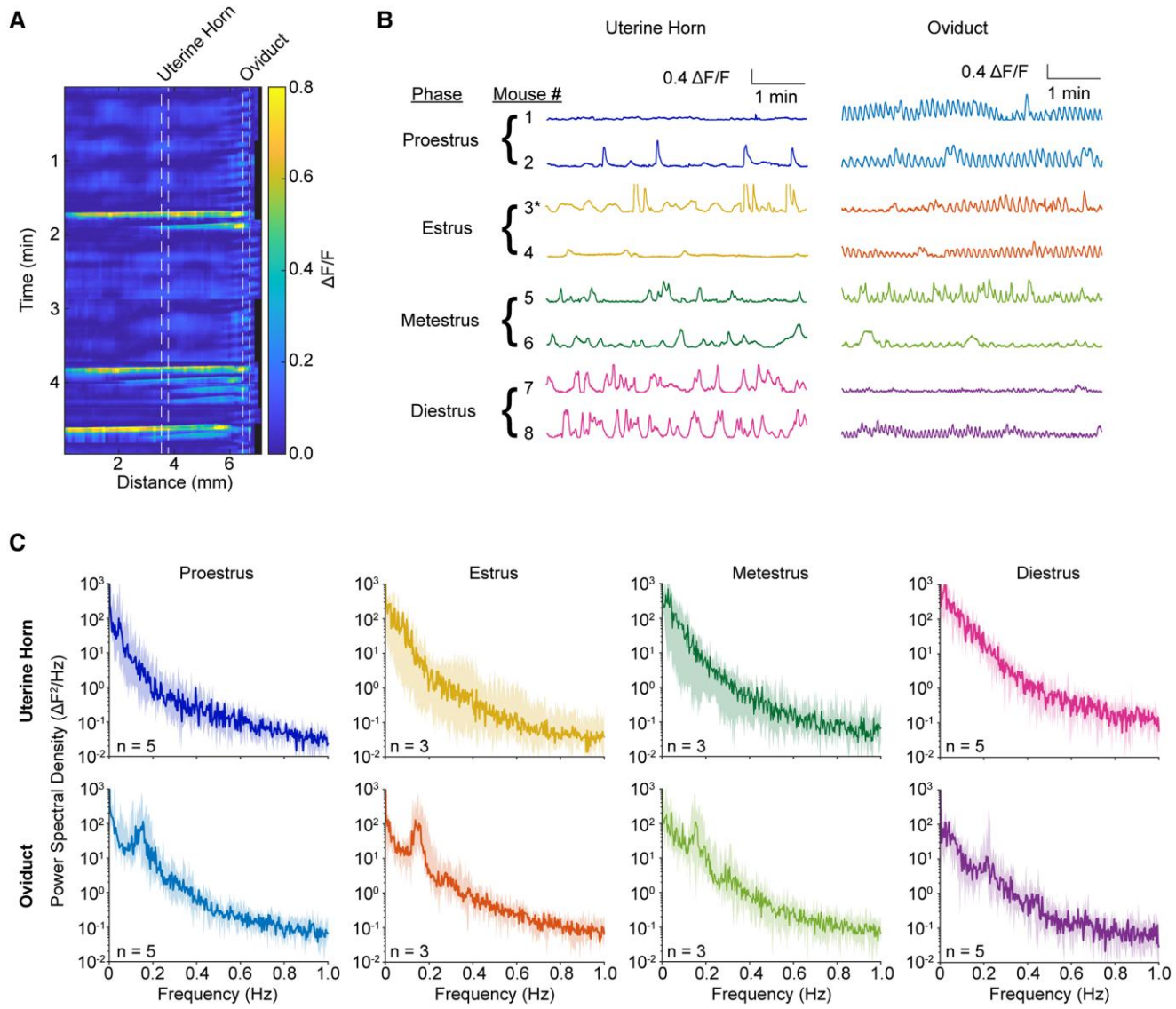

Fig. 4. Uterine calcium dynamics are not periodic. A) Kymograph with overlaid marks indicating regions analyzed for uterine horn and oviduct. B) Representative fluorescence traces from two mice in each estrous stage. Asterisks indicate traces derived from the kymograph in (A). C) Power spectral density of the uterine horn (Top panels) and oviduct (Lower panels) for each stage of estrous. The number of animals is marked on each panel.

McCarthy for technical advice on mouse surgery and uterine tissue dissection, and the Harvard Anesthesia Research Training Grant and the Harvard BIRCWH Program for their support (to D.J.C.).

Supplementary Material

Supplementary material is available at *PNAS Nexus* online.

Funding

This work was supported by an award from the Society for Obstetric Anesthesia and Perinatology, and by the NIH grants R01 HD037831 (to S.K.E.) K12 AR084230-20 (D.J.C.), and T32 GM007592-45 (D.J.C.).

Author Contributions

D.J.C.: conceptualization, software, formal analysis, investigation, methodology, writing—original draft, and writing—review and editing; E.M.M.: software, formal analysis, investigation, and methodology; S.K.E.: conceptualization, supervision, methodology, writing—original draft, and writing—review and editing; and A.E.C.: conceptualization, resources, software, formal analysis, supervision, methodology, writing—original draft, and writing—review and editing.

Preprint

This manuscript was posted on a preprint: https://doi.org/10.1101/2024.02.02.578395.

Data Availability

Data are available at the Harvard Dataverse: https://doi.org/10.7910/DVN/OFIB5S.

References

1 Malik M, Roh M, England SK. 2021. Uterine contractions in rodent models and humans. *Acta Physiol (Oxf)*. 231:e13607. https://doi.org/10.1111/apha.13607

2 Aguilar HN, Mitchell BF. 2010. Physiological pathways and molecular mechanisms regulating uterine contractility. *Hum Reprod Update*. 16:725–744. https://doi.org/10.1093/humupd/dmq016

3 Wray S, Arrowsmith S. 2021. Uterine excitability and ion channels and their changes with gestation and hormonal environment. *Annu Rev Physiol*. 83:331–357. https://doi.org/10.1146/annurev-physiol-032420-035509

4 Lammers WJEP. 2013. The electrical activities of the uterus during pregnancy. *Reprod Sci*. 20:182–189. https://doi.org/10.1177/1933719112446082

5 Talo A, Kärki AE. 1976. Electric activity of the rat myometrium in vivo during the estrous cycle. *Acta Physiol Scand*. 97:495–500. https://doi.org/10.1111/j.1748-1716.1976.tb10289.x

6 Ishikawa M, Fuchs AR. 1978. Electrical and mechanical activity of rat uterus in vivo during the estrous cycle. *Am J Obstet Gynecol*. 132:611–619. https://doi.org/10.1016/0002-9378(78)90852-9

7 Crane LH, Martin L. 1991. In vivo myometrial activity in the rat during the oestrous cycle: studies with a novel technique of video laparoscopy. *Reprod Fertil Dev*. 3:185–199. https://doi.org/10.1071/rd9910185

8 Griffiths AL, Marshall KM, Senior J, Fleming C, Woodward DF. 2006. Effect of the oestrous cycle, pregnancy and uterine region on the responsiveness of the isolated mouse uterus to prostaglandin F(2alpha) and the thromboxane mimetic U46619. *J Endocrinol*. 188:569–577. https://doi.org/10.1677/joe.1.06466

9 Wray S, Noble K. 2008. Sex hormones and excitation-contraction coupling in the uterus: the effects of oestrous and hormones. *J Neuroendocrinol*. 20:451–461. https://doi.org/10.1111/j.1365-2826.2008.01665.x

10 Dodds KN, Staikopoulos V, Beckett EAH. 2015. Uterine contractility in the nonpregnant mouse: changes during the estrous cycle and effects of chloride channel blockade. *Biol Reprod*. 92:141. https://doi.org/10.1095/biolreprod.115.129809

11 Ma X, *et al.* 2020. Microelectrode array analysis of mouse uterine smooth muscle electrical activity. *Biol Reprod*. 102:935–942. https://doi.org/10.1093/biolre/ioz214

12 Young RC. 2018. The uterine pacemaker of labor. *Best Pract Res Clin Obstet Gynaecol*. 52:68–87. https://doi.org/10.1016/j.bpobgyn.2018.04.002

13 Duquette RA, *et al.* 2005. Vimentin-positive, c-kit-negative interstitial cells in human and rat uterus: a role in pacemaking? *Biol Reprod*. 72:276–283. https://doi.org/10.1095/biolreprod.104.033506

14 Lutton EJ, Lammers WJEP, James S, van den Berg HA, Blanks AM. 2018. Identification of uterine pacemaker regions at the myometrial-placental interface in the rat. *J Physiol*. 596:2841–2852. https://doi.org/10.1113/JP275688

15 Smith R, Imtiaz M, Banney D, Paul JW, Young RC. 2015. Why the heart is like an orchestra and the uterus is like a soccer crowd. *Am J Obstet Gynecol*. 213:181–185. https://doi.org/10.1016/j.ajog.2015.06.040

16 Ren C, Komiyama T. 2021. Characterizing cortex-wide dynamics with wide-field calcium imaging. *J Neurosci*. 41:4160–4168. https://doi.org/10.1523/JNEUROSCI.3003-20.2021

17 Stevenson AJ, *et al.* 2020. Multiscale imaging of basal cell dynamics in the functionally mature mammary gland. *Proc Natl Acad Sci U S A*. 117:26822–26832. https://doi.org/10.1073/pnas.2016905117

18 Sanchez C, *et al.* 2021. Detection of Ca2+ transients near ryanodine receptors by targeting fluorescent Ca2+ sensors to the triad. *J Gen Physiol*. 153:e202012592. https://doi.org/10.1085/jgp.202012592

19 Hou JH, Kralj JM, Douglass AD, Engert F, Cohen AE. 2014. Simultaneous mapping of membrane voltage and calcium in zebrafish heart *in vivo* reveals chamber-specific developmental transitions in ionic currents. *Front Physiol*. 5:344. https://doi.org/10.3389/fphys.2014.00344

20 Jia BZ, Qi Y, Wong-Campos JD, Megason SG, Cohen AE. 2023. A bioelectrical phase transition patterns the first vertebrate heartbeats. *Nature*. 622:149–155. https://doi.org/10.1038/s41586-023-06561-z

21 Yang CF, *et al.* 2013. Sexually dimorphic neurons in the ventromedial hypothalamus govern mating in both sexes and aggression in males. *Cell*. 153:896–909. https://doi.org/10.1016/j.cell.2013.04.017

22 Arango NA, *et al.* 2008. A mesenchymal perspective of Müllerian duct differentiation and regression in Amhr2-lacZ mice. *Mol Reprod Dev*. 75:1154–1162. https://doi.org/10.1002/mrd.20858

23 McLean AC, Valenzuela N, Fai S, Bennett SAL. 2012. Performing vaginal lavage, crystal violet staining, and vaginal cytological evaluation for mouse estrous cycle staging identification. *J Vis Exp*. 67:e4389. https://doi.org/10.3791/4389

24 Kimura T, *et al.* 2019. Production of adeno-associated virus vectors for in vitro and in vivo applications. *Sci Rep*. 9:13601. https://doi.org/10.1038/s41598-019-49624-w

25 Robuck MF, *et al.* 2018. Monitoring uterine contractility in mice using a transcervical intrauterine pressure catheter. *Reproduction*. 155:447–456. https://doi.org/10.1530/REP-17-0647

26 Werley CA, Chien M-P, Cohen AE. 2017. Ultrawidefield microscope for high-speed fluorescence imaging and targeted optogenetic stimulation. *Biomed Opt Express*. 8:5794–5813. https://doi.org/10.1364/BOE.8.005794

27 Farhi SL, *et al.* 2019. Wide-area all-optical neurophysiology in acute brain slices. *J Neurosci*. 39:4889–4908. https://doi.org/10.1523/JNEUROSCI.0168-19.2019

28 Zhang Y, *et al.* 2023. Fast and sensitive GCaMP calcium indicators for imaging neural populations. *Nature*. 615:884–891. https://doi.org/10.1038/s41586-023-05828-9

29 Weinmann J, *et al.* 2020. Identification of a myotropic AAV by massively parallel in vivo evaluation of barcoded capsid variants. *Nat Commun*. 11:5432. https://doi.org/10.1038/s41467-020-19230-w

30 Soyal SM, *et al.* 2005. Cre-mediated recombination in cell lineages that express the progesterone receptor. *Genesis*. 41:58–66. https://doi.org/10.1002/gene.20098

31 Pierce SL, Kutschke W, Cabeza R, England SK. 2010. In vivo measurement of intrauterine pressure by telemetry: a new approach for studying parturition in mouse models. *Physiol Genomics*. 42:310–316. https://doi.org/10.1152/physiolgenomics.00058.2010

32 Jakobs MAH, Dimitracopoulos A, Franze K. 2019. KymoButler, a deep learning software for automated kymograph analysis. *Elife*. 8:e42288. https://doi.org/10.7554/eLife.42288

33 Dixon RE, Hwang SJ, Kim BH, Sanders KM, Ward SM. 2019. Myosalpinx contractions are essential for egg transport along the oviduct and are disrupted in reproductive tract diseases. *Adv Exp Med Biol*. 1124:265–294. https://doi.org/10.1007/978-981-13-5895-1_11

34 Zenclussen AC, Olivieri DN, Dustin ML, Tadokoro CE. 2013. In vivo multiphoton microscopy technique to reveal the physiology of the mouse uterus. *Am J Reprod Immunol*. 69:281–289. https://doi.org/10.1111/aji.12066

35 Zhang Y, *et al.* 2019. Analysis of in vivo uterine peristalsis in the non-pregnant female mouse. *Interface Focus*. 9:20180082. https://doi.org/10.1098/rsfs.2018.0082

36 Young RC. 2016. Mechanotransduction mechanisms for coordinating uterine contractions in human labor. *Reproduction*. 152: R51–R61. https://doi.org/10.1530/REP-16-0156

37 Mucenski ML, Mahoney R, Adam M, Potter AS, Potter SS. 2019. Single cell RNA-seq study of wild type and Hox9,10,11 mutant developing uterus. *Sci Rep*. 9:4557. https://doi.org/10.1038/s41598-019-40923-w

38 Thilander G, King GJ, Garfield RE. 1993. Connexin43 and gap junction content in the porcine myometrium during the estrous cycle. *Theriogenology*. 40:323–332.

39 Sheldon RE, *et al.* 2015. Functional and morphological development of the womb throughout life. *Science progress*. 98:103–127.

40 Dawson M, *et al.* 2024. Imaging the dynamics of murine uterine contractions in early pregnancy. *Biol Reprod*. 110:1175–1190. https://doi.org/10.1093/biolre/ioae071

41 Bertolin K, Murphy BD. 2014. 7—Reproductive tract changes during the mouse estrous cycle. In: Croy BA, Yamada AT, DeMayo FJ, Adamson SL, editors. *The guide to investigation of mouse pregnancy*. Boston: Academic Press. p. 85–94.

42 Hill-Eubanks DC, Werner ME, Heppner TJ, Nelson MT. 2011. Calcium signaling in smooth muscle. *Cold Spring Harb Perspect Biol*. 3:a004549. https://doi.org/10.1101/cshperspect.a004549

43 Gómez J, Ñeco P, DiFranco M, Vergara JL. 2006. Calcium release domains in mammalian skeletal muscle studied with two-photon imaging and spot detection techniques. *J Gen Physiol*. 127:623–637. https://doi.org/10.1085/jgp.200509475

44 Demmerle J, *et al.* 2017. Strategic and practical guidelines for successful structured illumination microscopy. *Nat Protoc*. 12: 988–1010. https://doi.org/10.1038/nprot.2017.019

45 Lim HJ, Wang H. 2010. Uterine disorders and pregnancy complications: insights from mouse models. *J Clin Invest*. 120:1004–1015. https://doi.org/10.1172/JCI41210

46 Weiss S, *et al.* 2006. Three-dimensional fiber architecture of the nonpregnant human uterus determined ex vivo using magnetic resonance diffusion tensor imaging. *Anat Rec A Discov Mol Cell Evol Biol*. 288:84–90. https://doi.org/10.1002/ar.a.20274

47 Bulletti C, *et al.* 2004. The patterns of uterine contractility in normal menstruating women: from physiology to pathology. *Ann N Y Acad Sci*. 1034:64–83. https://doi.org/10.1196/annals.1335.007

48 Kunz G, Leyendecker G. 2002. Uterine peristaltic activity during the menstrual cycle: characterization, regulation, function and dysfunction. *Reprod Biomed Online*. 4(Suppl 3):5–9. https://doi.org/10.1016/s1472-6483(12)60108-4

49 Kuijsters NPM, *et al.* 2017. Uterine peristalsis and fertility: current knowledge and future perspectives: a review and meta-analysis. *Reprod Biomed Online*. 35:50–71. https://doi.org/10.1016/j.rbmo.2017.03.019

50 Wang S, *et al.* 2024. Noninvasive imaging of 4D electrical activation patterns of uterine peristalsis during normal menstrual cycles. *NPJ Women's Health*. 2:1. https://doi.org/10.1038/s44294-023-00003-x

51 McCarthy R, *et al.* 2018. Mouse models of preterm birth: suggested assessment and reporting guidelines. *Biol Reprod*. 99: 922–937. https://doi.org/10.1093/biolre/ioy109

52 Dinulescu DM, *et al.* 2005. Role of K-ras and Pten in the development of mouse models of endometriosis and endometrioid ovarian cancer. *Nat Med*. 11:63–70. https://doi.org/10.1038/nm1173

53 Chadchan SB, *et al.* 2019. Antibiotic therapy with metronidazole reduces endometriosis disease progression in mice: a potential role for gut microbiota. *Hum Reprod*. 34:1106–1116. https://doi.org/10.1093/humrep/dez041

54 Prifti KK, *et al.* 2024. Obese mice have decreased uterine contractility and altered energy metabolism in the uterus at term gestation. *Biol Reprod*. 111:678–693. https://doi.org/10.1093/biolre/ioae086

55 Conover CA, *et al.* 2004. Metalloproteinase pregnancy-associated plasma protein A is a critical growth regulatory factor during fetal development. *Development*. 131:1187–1194. https://doi.org/10.1242/dev.00997

56 Ye X, *et al.* 2005. LPA3-mediated lysophosphatidic acid signalling in embryo implantation and spacing. *Nature*. 435:104–108. https://doi.org/10.1038/nature03505

57 Yokoi H, *et al.* 1994. High incidence of uterine inversion in mast cell-deficient osteopetrotic mutant mice of mi/mi genotype. *Biol Reprod*. 50:1034–1039. https://doi.org/10.1095/biolreprod50.5.1034

58 Tuo L, Tang S, Li S, Gu S, Xie Z. 2023. Murine models and research progress on dysmenorrhea. *Reprod Sci*. 30:2362–2372. https://doi.org/10.1007/s43032-023-01220-0